Available online at www.sciencedirect.com

ScienceDirect

Procedia CIRP 111 (2022) 832–837

www.elsevier.com/locate/procedia

12th CIRP Conference on Photonic Technologies [LANE 2022], 4-8 September 2022, Fürth, Germany

A novel approach for the quantitative characterization of shrink lines in the powder bed fusion of metals using a laser beam

Dominik Goetz[a]*, Daniel Wolf[a], Maja Lehmann[a], Michael F. Zaeh[a]

[a]*Institute for Machine Tools and Industrial Management (iwb), Technical University of Munich, Boltzmannstr. 15, 85748 Garching, Germany*

* Corresponding author. Tel.: +49 89 289-15485; fax: +49 89 289-15555. *E-mail address:* dominik.goetz@iwb.tum.de

Abstract

The powder bed fusion of metals using a laser beam (PBF-LB/M) enables the manufacturing of complex geometric designs with no part-specific tooling. As a result of the high energy input, the temperature gradients lead to a warpage of the part. Particularly at the structural transitions, thermally induced deformations form a shrink line on the outer surface of the geometry during PBF-LB/M. These shrink lines present a small notch, which reduces the dimensional accuracy and the part lifetime. However, the quantitative analysis of the shrink lines and their influencing factors has not been investigated yet. To specify the geometric characteristics of the shrink lines, a measurement approach is presented to enable their reliable and precise evaluation. A suitable test specimen was identified and varied within its geometrical dimensions. The results demonstrate the reproducible quantification of the shrink lines and their geometric characteristics. A significant dependence of the shrink lines on the geometry of the specimens is observed.

Peer-review under responsibility of the international review committee of the12th CIRP Conference on Photonic Technologies [LANE 2022]

Keywords: Powder bed fusion of metals using a laser beam (PBF-LB/M); shrink line; distortion; mesoscale; measurement

1. Introduction

The powder bed fusion of metals using a laser beam (PBF-LB/M) belongs to the Additive Manufacturing processes and is gaining an increasing relevance in various industries [1]. The main advantages are the customized manufacturing, the high geometric design freedom and the potential for functional integration [2,3]. In particular, this favors the fabrication of topology-optimized parts with free-form surfaces, thin-walled structures and structural transitions [4,5].

The manufacturing process uses a laser to selectively melt a metal powder and generates 3D geometries due to the layer-wise build-up process [6,7]. As a result of the local melting during PBF-LB/M, high temperature gradients occur. These lead to high thermally induced residual stresses and to the distortion of parts [8–10].

Especially at structural transitions with an increasing cross-section, a local deformation occurs on the outer surface of the part and forms a substantial notch [11]. These so-called *shrink lines* influence both the local warpage in the range of single layers (mesoscale) and the global warpage of the entire geometry (macroscale). Therefore, shrink lines are a significant challenge in terms of a reduced dimensional accuracy, resulting in an increased post-processing effort [12].

Hence, Adam and Zimmer [13] recommend avoiding structural transitions generally if they come along with an increasing cross-section. The higher cross-section leads to heat accumulations caused by a higher amount of the thermal energy. The avoidance of structural transitions cannot be guaranteed for topology-optimized geometries, as this would reduce the design freedom.

Kranz [14] indicated that shrink lines arise depending on the geometrical dimension of the part, such as the design of the structural transition. An explanatory model of the shrinkage-induced warpage at these geometric features was presented for PBF-LB/M, which is shown in Figure 1.

2212-8271
Peer-review under responsibility of the international review committee of the12th CIRP Conference on Photonic Technologies [LANE 2022]
10.1016/j.procir.2022.08.093

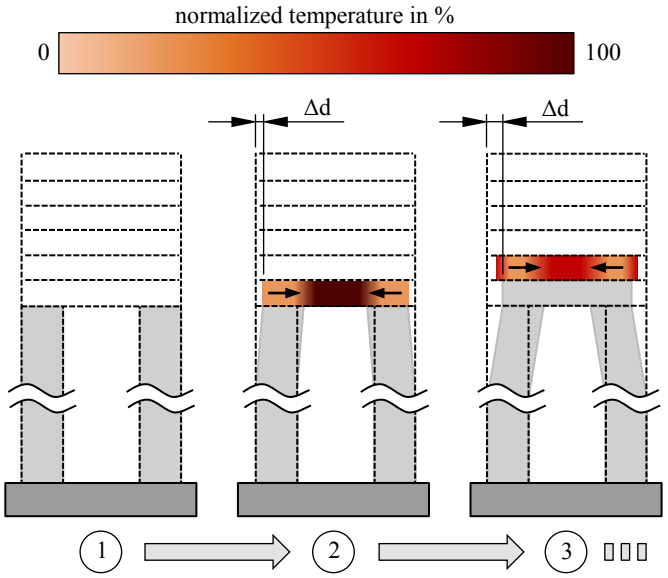

Fig. 1. Explanatory model of the formation procedure for the shrinkage-induced warpage at structural transitions (adapted from Kranz [14])

The shrink lines are caused at the structural transitions by a volume contraction of the single layers, which are created using only unsolidified powder underneath. This thermal contraction leads to tensile forces in the pillars, resulting in the distortion Δd and a notch on the outer surface. The notch might increase the likelihood of a crack initiation and therefore reduce the life time of the part [14]. With an increasing part height above the structural transition, the shrink line depth decreases due to the stronger material bond. Equally, the increasingly uniform heat dissipation causes lower tensile forces.

The formation of shrink lines was demonstrated through different geometries, which were characterized by a structural transition. However, quantitative measurements have not been carried out yet to specify the geometric shape of a shrink line. The quantitative evaluation of this mesoscale deformation still poses a challenge.

This paper aims at deriving a generally applicable method for measuring the shrink lines. Therefore, the distortion profile is divided into several zones, which enables a detailed analysis of the geometric dimensions.

2. Methods

Within this section, the manufactured specimens and the experimental setup are described. Based on these, the procedure of the optical measurement and the method for the reliable characterization of shrink lines are derived.

Table 1. Particle size distribution of the used material Inconel 718C

Diameter	D_{10} in µm	D_{50} in µm	D_{90} in µm
Value	18	30	46

Table 2. Process parameters used during PBF-LB/M

Parameter	Laser power in W	Laser speed in mm/s	Hatch distance in µm	Layer height in µm
Value	285	960	110	40

2.1. Experimental procedure

The shrink lines were triggered by a suitable specimen design. The geometry was adapted from Kranz [14] and comprised two pillars and one structural transition. Figure 2 shows the structural transition, which was specified by a 45° angle that blends into the radius r.

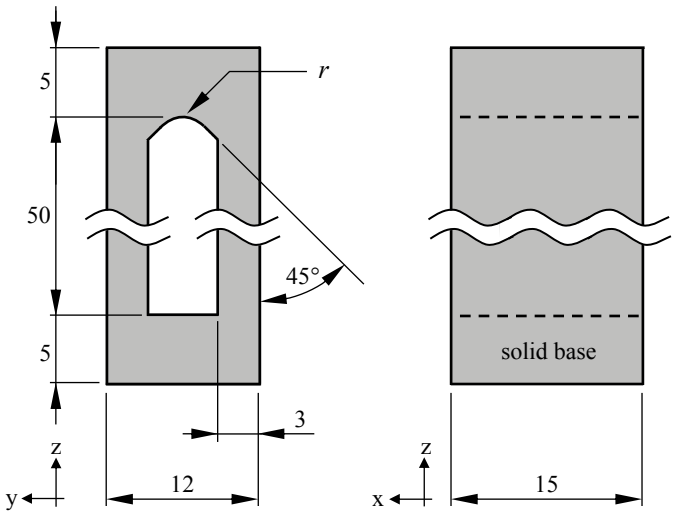

Fig. 2. Specimen design consisting of two pillars and one structural transition specified by the radius r

Within the experiments, the radius r was set to discrete values: $r_1 = 0$ mm, $r_2 = 1$ mm and $r_3 = 2$ mm. To prevent the pillars from an additional warpage during the separation from the build platform, a solid base was considered. Another solid region with a constant cross-sectional area was manufactured above the structural transition to stabilize the shrink line.

All specimens were processed on an EOS M400-1 machine (EOS GmbH). The nickel-based super alloy Inconel 718C (Oerlikon GmbH) was used as powder material. The particle size distribution of the metal powder is shown in Table 1.

The specimens were distributed randomly on the build platform (250 mm × 250 mm), which was mounted on an adapter plate. Additional parts were positioned on the build platform so that the layer time resulted in $t = 58$ s at the height of the structural transition (z = 55 mm). The specimens were arranged with a 5° angle to the recoating direction.

The exposure was realized with the process parameters shown in Table 2 and a stripe scanning strategy (67° rotation) against the gas flow direction. The specimens were manufactured three times with identical positions and process parameters.

2.2. Optical measurement

The optical 3D profilometer VR-3100 (Keyence Deutschland GmbH) was used with a 120× magnification to determine the distortion profile of the shrink line. The measurement was performed with an image composition and an automatic focus adjustment. The profilometer has an uncertainty of ± 3 µm in the y-direction and ± 2 µm in the x-z-plane. Figure 3 shows the arrangement of the measurement area to quantify the outer surface of the specimens.

To obtain a sufficient amount of data, at least 500 single measurement lines were performed. This requires a width of 5.0 mm with a maximum distance of 10 µm between the individual measurement lines. Hence, the measurement area of 7.0 mm × 5.0 mm was chosen for all specimens, centered in the depth direction (x-coordinate) of the specimen. The reference surface with a size of 2.5 mm × 3.5 mm was positioned above the shrink line. This avoids a distortion-related influence on the alignment of the surface profile. Therefore, the reference surface was located in the center and 0.5 mm from the top edge of the measurement area.

The reduction of single measurement peaks was carried out by smoothing the data with the *simple average* filter for a 3 pixels × 3 pixels square. Within the defined reference surface, the measurement of the surface roughness was conducted according to ISO 4288 [15]. The average distortion profile was calculated from the mean of the individual measurement lines. Within these experiments, one side of the manufactured specimens was measured.

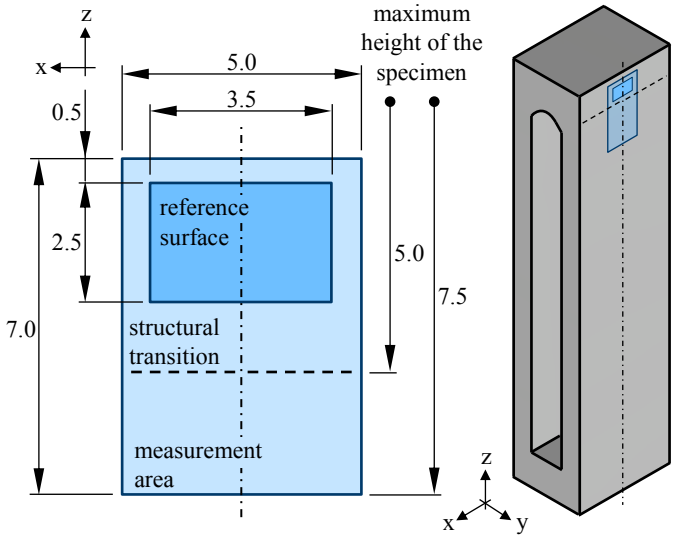

Fig. 3. Position and dimension of the measurement area for the evaluation of the shrink lines on the outer surface of the specimen

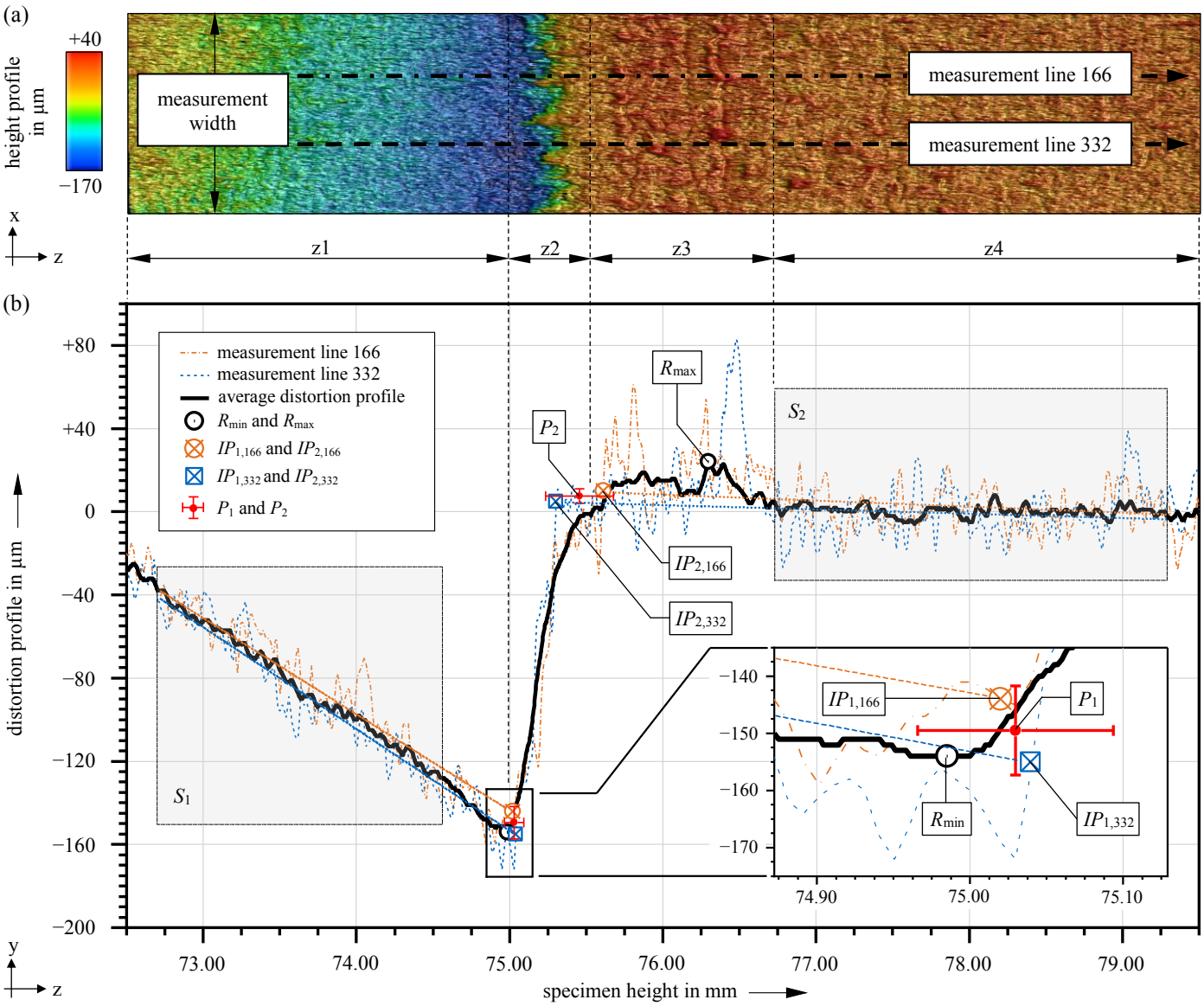

Fig. 4. (a) Height profile across the measurement width with two exemplarily shown individual measurement lines of a shrink line and the identified zones for the classification of the shrink line development and (b) the average distortion profile with the related position of the auxiliary points R_{min} and R_{max}, the interpolation sections S_1 and S_2, the intersection points IP_1 and IP_2 as well as the resulting points P_1 and P_2 for the quantitative analysis of a shrink line

2.3. Analysis algorithm

An objective method for the reproducible and precise evaluation of shrink lines was derived. Therefore, the profilometer data were prepared for the user-independent analysis. Defects resulting from undercut features in the optical measurement are interpolated linearly within the defined measurement area, provided that its size is $\leq D_{90}$ in the z-direction. Otherwise, the individual measurement lines are not included in the analysis algorithm.

In Figure 4, the height profile of an exemplary shrink line is shown with the associated distortion profile, which represents the mean across the individual measurement lines. Two individual measurement lines were analyzed to demonstrate the working principle of the analysis. Therefore, auxiliary points and intersection points were defined to characterize the dimension of the shrink line.

Based on the corresponding height profile and the model for the shrinkage-induced warpage, four zones (z1–z4) were identified to classify the development of the shrink line. In zone z1, the profile decreases linearly to a minimum value at the structural transition of the part, followed by a significant rise in zone z2. In this zone, an uneven increase is evident across the measurement width, which is reflected in the individual measurement lines (see Figure 4a). Zone z3 indicates the increasing sintering of powder particles. Their formation is hypothesized to originate from an overheating in the outer region of the warped specimen. In zone z4, the distortion remains constant above the shrink line. Throughout the whole profile, a fluctuation was identified resulting from the surface roughness.

The minimum value of the average distortion profile in zone z1 is defined by the auxiliary point R_{min} (see Figure 4b). Its position is confirmed by two successive conditions:

- A linear regression is performed through the former data points to verify the linear decrease of the distortion profile in zone z1. Therefore, a correlation coefficient $C \geq 0.80$ is required to ensure a high fit quality.
- The auxiliary point R_{min} needs to be located within a distance of D_{90} around this interpolated function, since the linear regression will not consider the influence of randomly adhering powder particles on the average distortion profile.

The interpolation section S_1 is arranged with a distance of five layers from the boundary of the measurement area and ten layers from the identified auxiliary point R_{min}. Analogously, the section S_2 is placed to the measurement border but limited by the beginning of zone z3.

Within the sections S_1 and S_2, a linear interpolation is performed on the data points for the individual measurement lines. By following the method in York et al. [16], the measurement uncertainty of the optical profilometer is considered in the interpolation. To determine the intersection points IP_1 and IP_2 farthest from the sections S_1 and S_2, the linear regression is extrapolated, taking into account the respective uncertainties. Thus, the influence of randomly adhering powder particles on the individual distortion profile is smoothed in the depth direction, which reduces the standard deviation in the analysis. The mean and standard deviation of the points P_1 and P_2 are calculated from the identified intersection points IP_1 and IP_2 across the individual measurement lines, respectively.

The shrink line height SLH and shrink line depth SLD are calculated by the determined points P_1 and P_2:

$$SLH = P_{2,z} - P_{1,z} \tag{1}$$

$$SLD = P_{2,y} - P_{1,y} \tag{2}$$

The standard deviation results from the statistically independent points P_1 and P_2 according to the law of *Gaussian error propagation:*

$$\sigma_{SLH} = \sqrt{\sum_{i=1}^{n}\left(\frac{\partial SLH}{\partial P_{i,z}} \cdot \sigma_{P_{i,z}}\right)^2} = \sqrt{{\sigma_{P_{1,z}}}^2 + {\sigma_{P_{2,z}}}^2} \tag{3}$$

$$\sigma_{SLD} = \sqrt{\sum_{i=1}^{n}\left(\frac{\partial SLD}{\partial P_{i,y}} \cdot \sigma_{P_{i,y}}\right)^2} = \sqrt{{\sigma_{P_{1,y}}}^2 + {\sigma_{P_{2,y}}}^2} \tag{4}$$

3. Results and discussion

The shrink line dimensions are evaluated by the proposed user-independent approach. In Figure 5, the standard deviation and the average distortion profile are presented exemplarily for the specimen with $r_3 = 2$ mm and its twofold repetition. To quantify the shrink lines, the determined points P_1 and P_2 as well as the zones z1–z4 are shown for the three build jobs.

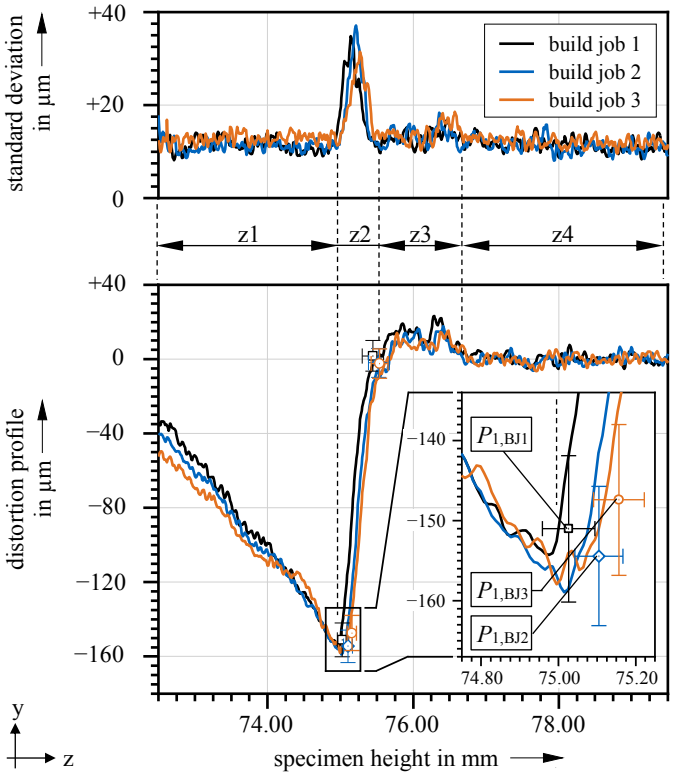

Fig. 5. Standard deviation and average distortion profile with the determined points P_1 and P_2 as well as the zones z1–z4 for the specimens with the radius $r_3 = 2$ mm across the three manufactured build jobs (BJ1–BJ3)

For the standard deviation, all values are below the permitted threshold $D_{90} = 46$ µm. The threshold results from randomly adhering powder particles in the individual measurement lines. It considers that when the material melts, neighboring powder particles are also bonded to the component due to the high energy input. A uniform progression ($\sigma \leq 19$ µm) was found in the zones z1, z3 and z4. In contrast, a maximum standard deviation $\sigma_{max} = 37$ µm was exhibited for the shrink lines in zone z2. This can be explained by the discontinuous increase as well as by the non-uniform start and end position of the shrink line across the measurement width, which is shown exemplarily in the height profile in Figure 4a.

In the average distortion profile, this effect also leads to the increased standard deviation $\sigma_{P_{1,z}}$ and $\sigma_{P_{2,z}}$ for the identified points P_1 and P_2 in the height direction of the specimen. The specific values are shown in Table 3.

Table 3. Standard deviations of the points P_1 and P_2 for the specimens with the radius $r_3 = 2$ mm at the structural transition

Parameter	$\sigma_{P_{1,z}}$ in µm	$\sigma_{P_{2,z}}$ in µm	$\sigma_{P_{1,y}}$ in µm	$\sigma_{P_{2,y}}$ in µm
Build job 1	68	147	9	8
Build job 2	62	145	9	8
Build job 3	65	118	9	8

Powder particles adhere randomly during the manufacturing process and influence the shrink line. Also, the discontinuous increase of the shrink line across the measurement width enlarges the standard deviation. Similarly, a minor error results during the measurement of the specimens. Due to the global warpage, they cannot be ideally aligned horizontally in the 3D profilometer. Clamping the specimens would additionally falsify the measurement due to the resulting distortion. Hence, a slight misalignment during the optical measurement, whose uncertainty is implicitly included in the determined standard deviation, is unavoidable.

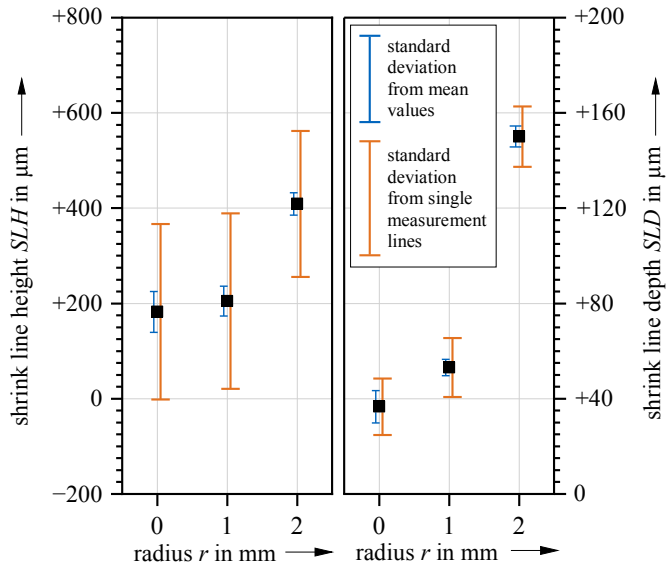

Fig. 6. Shrink line heights and depths of the specimens, shown with the standard deviation calculated from the mean values and the single measurement lines

In the depth direction, these effects were smoothed by extrapolating the sections S_1 and S_2. Hence, reduced standard deviations $\sigma_{P_{1,y}}$ and $\sigma_{P_{2,y}}$ result for P_1 and P_2 in the y-direction (see Table 3). The values are in the same order of magnitude as the surface roughness of the specimens, which was determined to be $Ra = 9 \pm 1$ µm within the defined reference surface. This confirms that locally adhering particles and the non-uniform rise in zone z2 influence the characterization of the shrink line height only.

However, the identified points P_1 and P_2 indicated a good agreement in their magnitude with regard to the mean values and their standard deviation for the three build jobs. This confirms the reproducibility of the shrink line as a mesoscale distortion effect.

It also indicates that the determined values are suitable for calculating the shrink line dimensions. In Figure 6, they are presented for the manufactured specimens, which differ in their radii at the structural transition.

As shown for the specimen with $r_1 = 0$ mm, the increased standard deviation of the points P_1 and P_2 can lead to the determination of a negative shrink line height. This is not physically meaningful because the layer-wise PBF-LB/M denies the influence on the previously manufactured layers. This can be explained by the unavoidable, slight misalignment of the specimen during the optical measurement. Nevertheless, an increasing shrink line height is indicated with a growing radius at the structural transition.

The same effect is observed for the shrink line depth. As the radius increases, the depth rises. Also, the standard deviations in the y-direction of the points P_1 and P_2 lead to a significantly lower standard deviation for the depth (see Table 3).

The trends are confirmed by the reduced standard deviation calculated from the specimen-specific mean shrink line heights and depths. This is explained by the previously performed averaging of the determined values within the individual measurement lines, which smoothes the influence of randomly adhering powder particles.

Hence, the geometry of the specimens indicated a significant influence on the formation of the shrink lines. A clear trend of the deformation is recognized in all evaluations. The results agree with the experimental investigations of Thomas [11] and Kranz [14], which were carried out with 316L stainless steel and Ti-6Al-4V, respectively. Although these were based on a purely qualitative evaluation of the geometric characteristics, it demonstrates the formation of shrink lines for materials with different crystalline structures.

The emergence of shrink lines has also been shown for different geometries. To enable their precise quantification for even complex surface shapes, the defined accuracy of the measurement data is required in order to select a suitable measuring tool. In dependence on the geometry, this may result in an adjustment of the dimensions of the measurement area and the reference surface. Nevertheless, the reference surface needs be placed in a shrink-line unaffected and plane area to ensure the analysis of the individual measurement lines. Following the presented approach, the characterization of shrink lines is enabled for arbitrary geometries.

4. Conclusions

The shrink lines result from a local distortion at the component junctions. To quantify the shrink lines, a novel approach for their characterization was presented. The procedure was applied to specimens with varying radii at the structural transition. In this paper, the following findings were derived:

- The shrink lines showed a reproducibility within a twofold repetition for the identical position on the build platform and the initially chosen process parameters.
- The analysis algorithm enables the quantification of the shrink line height and depth, which reduces the dimensional accuracy of the part.
- The determined depth and height of a shrink line increase with a growing radius at the structural transition.

To avoid negative shrink line heights for specimens without radii at their structural transitions, the misalignment during the optical measurement needs to be further minimized. Also, a specimen post-treatment, such as shot peening, will remove randomly adhering powder particles in future experiments and therefore reduce the standard deviations.

For a reliable prediction of shrink lines, the influence of geometrical and process-related parameters needs to be further investigated in the future.

Appendix A.

Analogously to Figure 5, the enlargement of the point P_2 is shown in Figure 7 with the standard deviation and the average distortion across the three build jobs.

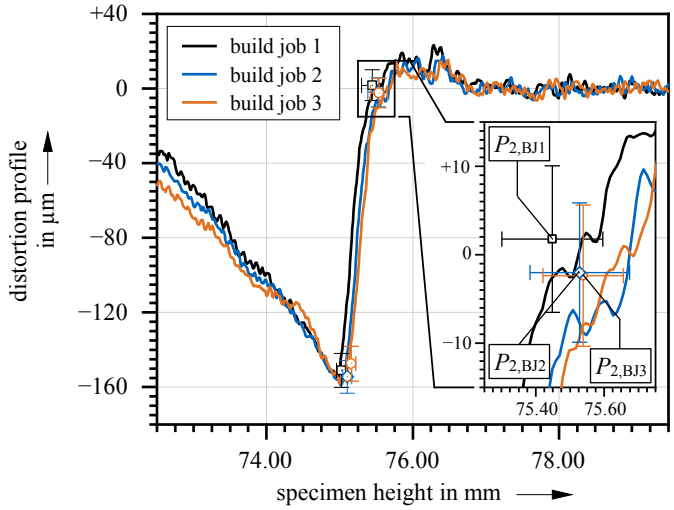

Fig. 7. Enlargement of the determined points P_2 with their respective mean values and standard deviations for the specimens with the radius $r_3 = 2$ mm across the three manufactured build jobs (BJ1–BJ3)

References

[1] Wohlers T, Campbell I, Diegel O, Kowen J, Mostow N. Wohlers Report 2021: 3D Printing and Additive Manufacturing State of the Industry. Fort Collins: Wohlers Associates; 2021.
[2] Alfaify A, Saleh M, M Abdullah F, Al-Ahmari A. Design for additive manufacturing: A systematic review. Sustainability 12(19), 7936. 2020.
[3] Yaghi A, Ayvar-Soberanis S, Moturu S, Bilkhu R, Afazov S. Design against distortion for additive manufacturing. Additive Manufacturing 27. 2019. pp. 224–235
[4] Liu J, Gaynor A, Chen S, Kang Z, Suresh K, Takezawa A, Li L, Kato J, Tang J, Wang C, Cheng L, Liang X, To A. Current and future trends in topology optimization for additive manufacturing. Structural and Multidisciplinary Optimization 57. 2018. pp. 2457–2483
[5] Meng L, Zhang W, Quan D, Shi G, Tang L, Hou Y, Breitkopf P, Zhu J, Gao T. From topology optimization design to additive manufacturing: Todays success and tomorrows roadmap. Archives of Computational Methods in Engineering 27. 2020. pp. 805–830
[6] Fateri M, Gebhardt A. 3D Printing of Optical Components – Introduction to Additive Manufacturing. Cham: Springer International Publishing; 2021. pp. 1–22
[7] Kruth JP. Material incress manufacturing by rapid prototyping techniques. CIRP Annals 40(2). 1991. pp. 603–614.
[8] Bartlett JL, Li X. An overview of residual stresses in metal powder bed fusion. Additive Manufacturing 27. 2019. pp.131–149
[9] Mercelis P, Kruth JP. Residual stresses in selective laser sintering and selective laser melting. Rapid Prototyping Journal 12. 2006. pp. 254–264
[10] Zaeh M, Branner G. Investigations on residual stresses and deformations in selective laser melting. Production Engineering 4. 2009. pp. 35–45
[11] Thomas D. The development of design rules for selective laser melting. PhD thesis, University of Wales Institute Cardiff. 2009
[12] Deradjat D, Minshall T. Implementation of rapid manufacturing for mass customisation. Journal of Manufacturing Technology Management 28(1). 2017. pp. 95–121
[13] Adam G, Zimmer D. Design for additive manufacturing: element transitions and aggregated structures. CIRP Journal of Manufacturing Science and Technology 7(1). 2013. pp. 20–28
[14] Kranz J. Methodik und Richtlinien fuer die Konstruktion von laseradditiv gefertigten Leichtbaustrukturen. Springer Vieweg, Berlin, Heidelberg. 2017.
[15] European Committee for Standardization. Geometrical product specifications (gps) – surface texture: Profile method – rules and procedures for the assessment of surface texture (iso 4288 : 1996). Standard. Brussel; 1996.
[16] York D, Evensen N, Martinez M, Delgado J. Unified equations for the slope, intercept, and standard errors of the best straight line. American Journal of Physics 72(3). 2004. pp. 367–375